

Topological textures and emergent altermagnetic signatures in ultrathin BiFeO₃

George Fratian^{1,22}, Maya Ramesh^{2,22}, Xinyan Li^{3,4,22}, Evangelos Golias⁵, Yousra Nahas⁶, Sebastian Maria Ulrich Schultheis⁷, Julian Skolaut⁷, Marti Checa⁸, Arundhati Ghosal¹, Jan Priessnitz⁹, F. C. Fobasso Mbognou⁹, Shashank Kumar Ojha^{3,4}, Shiyu Zhou¹⁰, Alexander Qualls¹, Kai Litzius¹¹, Christoph Klewe¹², Peter Meisenheimer¹³, Laurent Bellaiche^{6,14}, Libor Šmejkal^{9,15,16}, Darrell G. Schlom^{2,17,18}, Yimo Han^{3,4,19}, Sergei Prokhorenko⁶, Ramamoorthy Ramesh^{13,20}, Paul Stevenson²¹, Angela Wittmann^{7,*}, Lucas Caretta^{1,10*}

¹*School of Engineering, Brown University, Providence, Rhode Island, USA*

²*Department of Materials Science and Engineering, Cornell University, Ithaca, New York, USA.*

³*Department of Materials Science and Nanoengineering, Rice University, Houston, TX 77005 USA*

⁴*Rice Advanced Materials Institute, Rice University, Houston, TX 77005 USA*

⁵*MAX IV Laboratory, Lund, Sweden*

⁶*Smart Ferroic Materials Center, Physics Department, Institute for Nano-science and Engineering, University of Arkansas, Fayetteville, Arkansas 72701, USA*

⁷*Institute of Physics, Johannes Gutenberg-University Mainz, Mainz, Germany*

⁸*Center for Nanophase Materials Sciences, Oak Ridge National Laboratory, Oak Ridge, TN, 37831, USA.*

⁹*Max Planck Institute for the Physics of Complex Systems, Nöthnitzer Str. 38, 01187 Dresden, Germany*

¹⁰*Department of Physics, Brown University, Providence, Rhode Island, USA*

¹¹*Experimental Physics V, Center for Electronic Correlations and Magnetism, University of Augsburg, Augsburg, Germany*

¹²*Advanced Light Source, Lawrence Berkeley National Laboratory, Berkeley, CA, 94720, USA.*

¹³*Department of Materials Science and Engineering, University of California, Berkeley, California, 94720, USA*

¹⁴*Department of Materials Science and Engineering, Tel Aviv University, Ramat Aviv, Tel Aviv 6997801, Israel*

¹⁵*Max Planck Institute for Chemical Physics of Solids, Nöthnitzer Str. 40, 01187 Dresden, Germany*

¹⁶*Institute of Physics, Czech Academy of Sciences, Cukrovarnická 10, 162 00 Praha 6, Czech Republic*

¹⁷*Kavli Institute at Cornell for Nanoscale Science, Cornell University, Ithaca, NY, USA*

¹⁸*Leibniz-Institut für Kristallzüchtung, Berlin, Germany*

¹⁹*Smalley-Curl Institute, Rice University, Houston, TX 77005, USA*

²⁰*Department of Physics, University of California, Berkeley, California, 94720, USA*

²¹*Department of Physics, Northeastern University, Boston, MA 02115 USA*

²²*These authors contributed equally.*

*Correspondence to: luca_caretta@brown.edu, a.wittmann@uni-mainz.de

Abstract

Magnetoelectric multiferroics, materials with intrinsically coupled electric polarization and magnetic order, promise ultralow-power switching, nonvolatile memory, and energy-efficient signal transduction. Yet practical deployment demands ultrathin films down to the atomic limit, where both orders typically degrade. Maintaining both order parameters at the thinnest scales in complex oxides remains a tremendous challenge, as uncompensated bound charge drives nanoscale depolarization in most ferroelectrics, while off-stoichiometry, reduced anisotropy, and charge transfer can produce magnetic dead layers in ultrathin oxides at substrate interfaces. Here, we realize a multiferroic phase of BiFeO₃ that not only sustains both order parameters at room temperature with no dead layer but also exhibits signatures of emergent altermagnetism in the four-unit-cell, ultrathin limit. First-principles calculations, spin symmetry analysis, atomic-resolution imaging, and angle-resolved magnetic imaging reveal that short-circuit electrostatic boundary conditions, together with epitaxial

strain, drive a continuous second-order, thickness-driven phase transition that enables the formation of multiferroic topological textures. Moreover, the imposed boundary conditions stabilize a d-wave altermagnetic time-reversal symmetry breaking, with corresponding signatures observed in magnetic circular dichroism. Collectively, these results establish a pathway to stabilize unconventional multiferroicity at device-relevant thicknesses, reframing scaling limits for oxide electronics.

Introduction

Correlated thin film materials often suffer from loss of functionality at the thinnest length scales due to interface/surface effects, dimensionality, chemical intermixing, or even strain. This challenge is particularly pervasive in ferroic complex oxide perovskites. As an example, magnetic dead layers are well-known in manganites¹⁻³ due to structural distortions and changes in electronic states at interfaces. In ferroelectric films, large depolarizing fields from uncompensated bound charge suppress polarization, such as in ultrathin $\text{Pb}(\text{Zr}_x\text{Ti}_{1-x})\text{O}_3$ ⁴⁻⁹. Multiferroic BiFeO_3 (BFO) is no exception to unfavorable thickness scaling, where both the antiferromagnetism and switchable polarization are reported to vanish below approximately ten unit cells^{10,11}. This occurs primarily due to strong depolarizing electric fields resulting from BFO's large out-of-plane ferroelectric polarization and loss of magnetic anisotropy. These challenges in scaling have hindered the use of BFO in microelectronic technologies, as thinner multiferroic materials are desired for favorable low voltage devices. Several strategies have been pursued to combat scaling issues in BFO and other magnetic or ferroelectric oxides to retain ferroic order in the ultrathin regime. These include electrostatic techniques^{7,12-16}, chemical termination at ferroelectric interfaces^{17,18}, and confinement in superlattice structures¹⁹. Furthermore, to prevent magnetic dead layer formation, proximity/geometric effects^{20,21} and strain²² have been proposed as engineering strategies. Despite these efforts, however, maintaining multiferroic functionality of BFO at the thinnest length scales remains a fundamental challenge, as cooperative design of ferroelectric and magnetic order in multiferroics is challenging.

Here, we apply an atomic-scale design strategy that utilizes short-circuit boundary conditions and compressive strain induced by substrate-film lattice mismatch to stabilize ferroelectric order in BFO with no dead layer (often referred to as having no critical ferroelectric thickness) and magnetic order down to at least 4 unit cells. Surprisingly, we find that at thicknesses less than ~3 nm, BFO undergoes a continuous

structural and ferroic phase transition which favors preferential out-of-plane polarization and coincides with the emergence of topological multiferroic textures. This rarely reported, emergent phase of BFO – stabilized by the epitaxial boundary conditions – exhibits properties and symmetries indicative of altermagnetism, as suggested by first-principle calculations and angle-resolved X-ray dichroism. The stabilization of multiferroic order, topology, and altermagnetic signatures at the ultrathin limits provides a pathway for low power integration of BFO into beyond-CMOS computing paradigms.

Thickness induced phase transformation and retained polar order

To retain polar and magnetic order in the ultrathin regime, we employ two design strategies. First, to mitigate adverse electrostatics and suppress depolarizing fields, we synthesize BFO on a lattice matched oxide electrode whose free electrons provide efficient electronic screening. Second, we impose large epitaxial compressive strain via growth on a lattice mismatched substrate to stabilize out-of-plane structural distortions and, consequently, out-of-plane polarization. We realize both by synthesizing BFO thin films on (110)-oriented DyScO_3 (DSO) substrates with 20 nm thick SrRuO_3 (SRO) bottom electrodes using reactive oxide molecular-beam epitaxy, which promotes stoichiometric control and minimizes sample defects (Methods). Although the BFO/SRO//DSO heterostructure has been widely studied in various contexts, the mismatch in octahedral tilt patterns between BFO and SRO can induce interfacial structural frustration that becomes dominant at sufficiently small thicknesses, with implications for the thickness scaling of ferroic order^{23–29}.

High-angle annular dark-field scanning transmission electron microscopy (HAADF-STEM) images of a heterostructure containing a four-unit-cell-thick BFO layer (Fig. 1a,b), acquired along the $[1\bar{1}0]_0$ and $[001]_0$ zone axes of the DSO substrate (O denotes orthorhombic), demonstrate single crystal films with atomically sharp interfaces between layers. Single phase films and atomically smooth surfaces are confirmed with X-ray diffraction and atomic force microscopy (Extended Data Figs. 1 and 2). To confirm the precise polar order in the BFO layer, multislice electron ptychography (MEP) was performed to obtain super-resolution phase images for polar mapping (Fig. 1a,b, Methods). Remarkably, relative to bulk or thicker BFO films, where BFO adopts a rhombohedral $R\bar{3}c$ structure with spontaneous ferroelectric

polarization \mathbf{P} aligned along $<111>_{\text{PC}}$ (PC denotes pseudocubic), the ultrathin films exhibit a modified symmetry with an *enhanced* out-of-plane-to-in-plane polarization ratio, precisely where depolarizing fields are typically largest. This effect is most pronounced along the more compressed $[1\bar{1}0]_0$ DSO zone axis, where the film exhibits a purely out-of-plane $[001]_{\text{PC}}$ polarization, as indicated by cation atomic displacements across the BFO/SRO interface shown in Fig. 1c,d. Notably, we observe no ferroelectric dead layer in the BFO, implying that the first deposited unit cell under these boundary conditions is polar. Moreover, along both zone axes, BFO also induces symmetry breaking (cation displacement) in the adjacent SRO underlayer consistent with a polar metal, which may in turn help stabilize the ferroelectric state in the first unit cell of BFO³⁰. Additional STEM imaging of other BFO thicknesses is shown in Extended Data Figs. 3 and 4. We emphasize that these structural distortions in BFO and SRO at the BFO/SRO interface are exclusively observed in the thinnest BFO samples and differ from their typical bulk phases (Extended Data Figs. 4 and 5). Hysteresis loops using a quadrature phase differential interferometer (QPDI)-based piezoresponse force microscopy (PFM) are also shown in Extended Data Fig. 6 and are indicative of switching behavior.

To better understand the origin of the observed BFO structure, we have performed density functional theory (DFT) simulations for bulk BFO and BFO/SRO bilayer geometries (Methods). The former case serves as a benchmark representing an ideal screening scenario. Here, we partially account for ultra-thin film conditions by fixing the experimental values of epitaxial strain and $c/a=1.02$ ratio, as well as seeding structural relaxation with different ionic positions compatible with our HAADF-STEM observations (Figs. 1e-f). In the second scenario, we consider a BFO/SRO bilayer comprising six u.c. layers of SRO and four u.c. layers of BFO. The top atomic plane of BFO is interleaved with the bottom-most Ru-O plane by a 30 Å vacuum slab and dipolar corrections are introduced to minimize periodic boundary condition artifacts. Such setup portrays a scenario where the screening of polarization in BFO is provided only by the SRO buffer and attempts to faithfully account for most of the interfacial effects.

The described bulk scenario relaxation yields either an M_a or M_c monoclinic BFO phase with polarization lying within the $(1\bar{1}0)_{\text{PC}}$ and $(100)_{\text{PC}}$ planes, respectively. The absence of polarization along

the $[100]_{\text{PC}}$ axis in the M_c phase makes it a close match to the experimentally observed structure. The unit cell has a Cm space-group symmetry and is shown in Fig. 1g. In addition to polar displacements, it features anti-phase oxygen octahedra rotations along the $[010]_{\text{PC}}$ and $[001]_{\text{PC}}$ axes, giving rise to a $a^0b^{\circ}c^{\circ}$ tilt pattern. The absence of antiferro distortions (AFD) along the $[100]_{\text{PC}}$ direction is also consistent with our experiments (Fig. 1f). The distortions with respect to the cubic $Pm\bar{3}m$ structure are dominated by the polar Γ_4^- and the antiferrodistortive R_5^- mode as well as a lesser magnitude anti-polar R_4^- motion of Bi ions. At the same time, the energy of the M_c phase is 42 meV/u.c. higher compared to its rhombohedral-like M_a counterpart, and lifting symmetry constraints renders M_c unstable. Further unconstrained relaxation leads to a rapid development of an additional polarization component along $[100]_{\text{PC}}$ resulting in either a triclinic or monoclinic M_a phase. This result points to the importance of additional interfacial structural constraints required to stabilize the observed M_c BFO structure.

In the bilayer setup, we do not impose any symmetry constraints during the relaxation but fix the geometry of the three bottom-most unit cells of the SRO slab to mimic a thicker SRO buffer (Methods). Similarly to the bulk case, our bilayer simulations also predict multiple metastable minima. The only relaxed structure reproducing the two-component polarization of the grown samples (Figs. 1b-c) and AFD-like O_6 distortion (Fig. 1e) closely resembles the bulk M_c phase described above. However, this time, the magnitude of polar and AFD distortions is inhomogeneous across the BFO thickness – both in-plane and out-of-plane displacements gradually increase upon approaching the top interface of the BFO layer. The calculated polar displacements of B-site ions are reported in Extended data Fig. 7, showing good qualitative agreement with our experimental results. Additionally, similar to Fig. 1d, our calculations show an enhanced ratio of the out-of-plane to in-plane polarization at the top BFO surface. We attribute this effect to the breaking of the out-of-plane mirror symmetry intrinsic to most planar interfaces. Such breaking inevitably gives rise to an interfacial dipole driving the top atomic layers of BFO towards a more tetragonal-like polarization state. Our simulations thereby confirm that the SRO buffer provides enough screening to ensure a stable out-of-plane polarization for atomically thick BFO films. Regarding the symmetry, earlier studies have suggested that the monoclinic M_c , rarely observed in BFO, is a transient state along the R - M_a -

M_c - T path bridging the rhombohedral R and tetragonal T phases^{31,32}. In our case, the nominally rhombohedral BFO is driven towards the T state by a combination of a moderate compressive strain and structural boundary conditions. The former, epitaxial strain, suffices to stabilize the M_a phase. The latter conditions include strong out-of-plane forces at the top BFO/vacuum interface as well as constrained O₆ tilts at the BFO/SRO interface. These constraints guide the system further along the R - M_a - M_c - T path, giving rise to an M_c phase with Cm symmetry.

Magnetic order in ultrathin BFO

Having established boundary conditions that stabilize polar order down to the first unit cell, we next examine how these conditions, and the associated structural phase transition, affect the magnetic properties in ultrathin BFO. In bulk or thin film BFO, the ferroelectric polarization induces a strong Dzyaloshinskii–Moriya interaction (DMI) that typically results in a long-wavelength, incommensurate spin cycloid oriented along $\langle 1\bar{1}0 \rangle_{PC}$ or $\langle 11\bar{2} \rangle_{PC}$ perpendicular to \mathbf{P} ^{33–35}, often referred to as Type-I or Type-II cycloids, respectively. The cycloid propagation vector is known to be tunable via epitaxial strain, electrostatic boundary conditions, and applied electric fields^{36,37}, i.e. sensitive to crystallographic perturbations. As our engineered boundary conditions stabilize a unique phase of BFO, it could be expected that the magnetic structure is significantly different than in bulk. To probe how the imposed boundary conditions modify magnetic order in ultrathin BFO, we employ X-ray linear dichroism (XLD) in total electron yield mode and scanning nitrogen-vacancy center (NV) magnetometry. First, we use XLD with differential polarization contrast (Methods). In BFO, linear dichroism signal can be sensitive to both AFM and polar order depending on the chosen elemental resonance^{38–40}. Specifically, we measure at the Fe L₂-edge, where linear dichroism in BFO is predominantly sensitive to AFM order as sensitivity to polar order is largely diminished (see Supplementary Discussion I and Extended Data Figs. 8–10 for details on XLD sensitivity in BFO). Figures 2a–c present the Fe L₂-edge XLD intensity as a function of BFO thickness in BFO/SRO//DSO heterostructures for several crystallographic directions (see insets; additional datasets in Extended Data Fig. 11). First, we measure under grazing-incidence illumination (16° relative to the sample

plane), with X-rays incident along $[1\bar{1}0]_0$ substrate direction and *s*- and *p*-polarized light oriented parallel and perpendicular to the sample plane, respectively (Fig. 2a inset). Here, Fe L₂-edge XLD signal is reduced for thicknesses below \sim 10 nm (Fig. 2a), consistent with prior reports on BFO at these scales¹⁰. However, by contrast, the XLD intensity along $[001]_0$ – the more compressively strained direction – significantly *increases* for BFO films thinner than \sim 10 nm (Fig. 2b). Taken together, these trends indicate that AFM order persists at the thinnest length scale (rather than being completely suppressed) with stronger magnetic anisotropy rotating towards $[001]_0$ in the ultrathin limit.

STEM imaging shows that the polarization is largely out of plane in the ultrathin regime. As normal-incidence XLD does not detect out-of-plane polar order, this enables us to rule out a significant ferroelectric contribution to the signal. Normal-incidence XLD data is shown in Fig. 2c, confirming this pronounced in-plane AFM anisotropy along $[001]_0$ with a Néel temperature near 500 K in 1.6 nm (4 u.c.) thick films and 350 K in 0.4 nm (1 u.c.) thick films (Extended Data Fig. 12). The continuous, thickness-dependent rotation of the magnetic easy axis is consistent with a second-order phase transformation that coincides with the structural transition observed by TEM.

A pronounced evolution of magnetic order at ultrathin thickness is confirmed by nanoscale scanning NV magnetometry⁴¹ (Methods; Fig. 2d). In films \geq 10 nm, the NV mapping shows the now characteristic zigzag pattern of a Type-I spin cycloid in BFO, consistent with prior reports^{36,41,42}. At 5 nm, near the thickness-driven structural transition, vestiges of a periodic cycloidal texture remain, but the propagation length is markedly reduced, and a clear zigzag pattern is absent. At 1.6 nm (four unit cells), the NV signal lacks cycloidal signatures and instead reflects weak ferromagnetism or canted AFM order. By examining the persistence of the long-range order via a Fast Fourier Transform across the thickness series (see Extended Data Fig. 13), these results confirm that magnetic order persists to the ultrathin limit and that the cycloid is suppressed at these length scales as BFO undergoes the structural phase transformation.

Topological multiferroic defects across a continuous phase transition

To further resolve the local evolution of ferroelectricity and magnetism through the thickness-driven phase transformation, we map domain structures using angle-resolved XLD photoemission electron

microscopy (PEEM, Methods). Contrasting with above, XLD-PEEM images were acquired at the Fe L₃-edge, which in addition to providing higher signal in BFO, gives contrast from both polar and magnetic order³⁸⁻⁴⁰, as confirmed in our measurements (Supplementary Discussion I; Extended Data Figs. 8-10). Images were acquired under normal-incidence X-ray illumination, which probes in-plane projections of polar and AFM components. Figures 3a-c show XLD PEEM vector maps at representative BFO thicknesses – 50 nm, 3.5 nm, and 1.6 nm – spanning the structural phase transition. Images were acquired every ~10 degrees to construct the vector map (Methods). In 50 nm thick films under these boundary conditions, BFO is expected to relax into a striped ferroelectric domain pattern separated by 71° ferroelectric domain walls²³. Consistent with this, Fig. 3a displays alternating red/blue contrast from the in-plane component of the striped polar order, and piezoresponse force microscopy images (Extended Data Fig. 14), as well as Oxygen K-edge XLD^{39,40} (Supplementary Discussion I; Extended Data Figs. 8-10) corroborate that these stripes correspond to ferroelectric domains. We note that 180° domains exhibit identical contrast levels and are indistinguishable via XLD alone. The spin cycloid is not resolved at this thickness despite its appearance in NV magnetometry imaging (Fig. 2d), indicating that the XLD contrast in this thick 50 nm is dominated by the in-plane component of ferroelectric order in the thick-film limit. Radial histograms are shown in Fig. 3d and Extended Data Fig. 8 and quantify the angular distribution of XLD contrast, where red/blue indicates ferroelectric order, while purple/white indicates AFM order. The histograms confirm ferroelectric-dominated signal (red/blue) in thick BFO (Supplementary Discussion II). Nevertheless, pronounced magnetic contrast (purple/white) appears locally near ferroelastic domain boundaries, consistent with emergent magnetic behavior at BFO domain walls reported elsewhere^{36,40-45}.

At reduced thickness, midway through the structural phase transition, BFO undergoes pronounced domain reconfiguration, as seen in the 3.5-nm XLD-PEEM map (Fig. 3b). The ferroelectric pattern (red/blue) loses its long-range stripe character and becomes mosaic-like, no longer resembling the ordered stripes observed in thicker films. The normal-incidence imaging geometry only probes in-plane components; consequently, as the polarization rotates toward the out-of-plane direction [001]_{PC} (Figs. 1a,b), AFM moments rotate in-plane, since they are fixed normal to **P**, resulting in a reduction of the ferroelectric

contrast and an underlying magnetic texture that emerges. Short-range purple/white stripes within each polar domain trace the in-plane component of the spin-cycloid Néel vector, with a periodicity of \sim 58 nm (Extended Data Fig. 15), consistent with prior reports for BFO^{36,41,42,46}. The \sim 90° rotation of the projected spin cycloid between neighboring ferroelectric domains is also consistent with the Type-I cycloid expected in BFO^{36,41,42}, as the cycloid propagation vector \mathbf{k} is locked to the ferroelectric domain orientation (i.e., for a given \mathbf{P} , \mathbf{k} remains fixed), indicating retained magnetoelectric coupling at this thickness. Notably, here we resolve the spin cycloid in BFO using standard XLD PEEM imaging, circumventing more complicated techniques and sample preparation, such as in soft X-ray ptychography⁴⁰. Significantly, at the boundaries between mosaic ferroelectric domains, polar and magnetic order become frustrated, producing a rich landscape of topological multiferroic textures (pink and green boxes in Fig. 3b). Enlarged vector maps of representative textures are shown in Fig. 3c–e with accompanying schematics. The local vorticity, defined as $\boldsymbol{\omega} = \nabla \times \mathbf{u}$ with \mathbf{u} the order-parameter field (polar or Néel), is finite in these regions, yielding vortex-like and vortex-ring configurations comprising of both polarization and AFM order, whose finite winding corresponds to a nonzero topological charge. The emergence of these thickness-driven textures is consistent with Kibble–Zurek physics, where a continuous transition “freeze in” domains of polar and Néel order that later unwind into vortical configurations^{47,48}, also seen in other AFMs⁴⁹. Notably, within these frustrated multiferroic regions, \mathbf{P} and \mathbf{k} are not directly correlated; instead, they appear to jointly constitute the topological textures.

At 4 unit cells thickness (1.6 nm), the phase transformation is complete, rendering a distinct XLD vector map. At this thickness, \mathbf{P} is predominately out-of-plane, yielding diminished in-plane polar contrast and signal that is dominated by the in-plane component of the magnetization (purple/white in Fig. 3f). However, unlike thicker films, this phase of BFO does not contain cycloidal order, but rather appears to be a canted *collinear* AFM order that is highly anisotropic in nature. As expected from macroscopic XLD measurements (Fig. 2), AFM domains predominately have Néel vector orientations along [100]_{PC} (purple) and AFM anti-phase domain walls along [010]_{PC} (white) separating these domains. This domain pattern is similar to that measured in hematite (α -Fe₂O₃), the parent compound of BFO, near its Morin transition^{49,50}.

Emergent altermagnetic signature in ultrathin BFO

By establishing boundary conditions that eliminate the dead layer in BFO, we reveal a previously hidden non-cycloidal magnetic state. In conventional bulk BFO, nonrelativistic spin splitting has been predicted for several stable phases, provided that collinear magnetic order is present, rather than cycloidal order commonly found in BFO⁵¹⁻⁵⁴. The suppression of the spin cycloid and reduction of crystal symmetry in our ultrathin phase of BFO is suggestive of emergent altermagnetic behavior. We use DFT to investigate the compatibility of the emergent structure with altermagnetism. Notably, we readily see altermagnetic signatures in our DFT simulations. At the collinear spins level, our calculations predict a G-AFM ground state ordering of Fe spins for the *Cm* BFO phase shown in Fig. 4a together with DFT calculations (see Methods) of the altermagnetic spin density. The computed altermagnetism spin density is consistent with our spin group theory analysis. The spin group generators include a combined symmetry of spin rotation and mirror plane⁵⁵ along the b-crystallographic direction, $[C_2||m_b]$ marked in Fig. 4a, and lattice centering operation $[E||E|(\% \ 0 \ 0)]$. The corresponding spin Laue group is $^22/m$ resulting in a bulk d-wave altermagnetism of B-2 class⁵⁵. The B-2 class d-wave altermagnetism in our *Cm* BFO is characteristic by an altermagnetic nodal plane protected by the $[C_2||m_b]$, and another nodal plane that is not enforced to be flat due to the low symmetry of the *Cm* BFO phase. This is distinct from the previously studied bulk BFOs with a predicted g-wave and i-wave altermagnetic spin splitting^{51,52}.

In Fig. 4b, we study the corresponding altermagnetic spin polarization and spin splitting in momentum space. The nonrelativistic (spin orbit coupling switched off) DFT calculations confirm the d-wave altermagnetic symmetry of spin polarization in our thin film *Cm* BFO as seen on the constant energy isosurface in the left panel of Fig. 4b. The right panel of Fig. 4b shows the corresponding alternating nonrelativistic spin splitting of the bands along the -*YTY'* and -*YTY* directions. The magnitude of the spin splitting is most noticeable in the vicinity of the valence band maximum reaching up to ~ 0.3 eV. This nonrelativistic spin splitting magnitude is largest among the hitherto predicted altermagnetic multiferroic candidates^{52,56}. The strong altermagnetism seen in our DFT calculations of *Cm* BFO indicated its crystallography being favorable for detecting the effects resulting from the altermagnetic time-reversal

symmetry breaking. This includes x-ray magnetic circular dichroism (XMCD) which is allowed in our structure and we discuss further.

As indicated in previous works for other potential altermagnets, X-ray spectroscopy dichroism can provide experimental insights into altermagnetic behavior⁵⁷⁻⁵⁹. To probe signatures of the altermagnetic time-reversal symmetry breaking, we use XMCD (Methods). Figures 4c and d plot co-registered local XLD vector and XMCD image from the same region of the four unit-cell (1.6 nm) film (Methods). Vector-XLD maps in Fig. 4c show the real space orientation of the compensated Néel vector configuration, while XMCD records the time-reversal symmetry breaking permitted by altermagnetic symmetry (see Supplementary Discussion III). In Fig. 4d, pronounced XMCD contrast emerges in the thinnest, collinear, monoclinic sample, whereas its presence is absent at all other thicknesses >1.6 nm when the spin cycloid is still present (see Extended Data Fig. 16, Supplementary Discussion III). We note that the monoclinic BFO's weak canted moment is predicted to be largely in-plane and thus falls outside the sensitivity of our out-of-plane XMCD geometry (Supplementary Discussion IV). XMCD contrast in the thinnest sample reverses between circularly left and circularly right polarization (Extended Data Fig. 16), indicative of true magnetic origin. As demonstrated elsewhere^{58,59}, combining the two channels through a logical (Boolean) reconstruction yields a full real-space map of the Néel vector, a capability that arises from the interplay between altermagnetic symmetry and Hall conductivity, and links real-space imaging to reciprocal-space band structure. Analogous to the Hall effect in transport measurements, XMCD can be cast in terms of a Hall pseudovector⁶⁰ with components, $\mathbf{h} = [\sigma_{zy} \sigma_{xz} \sigma_{yx}]$, where $\sigma_{ij} = -\sigma_{ji}$ are the antisymmetric components of the frequency-dependent conductivity tensor. In our system, the [100]_{PC} orientation (perpendicular to the mirror plane) of the Néel vector combined with the observed BFO structure (Fig. 1) is compatible with the *Cm'* magnetic symmetry or *m'* magnetic point group. The latter allows for the Hall pseudovector lying within the mirror plane (see Fig. 4a) containing ferroelectric polarization. While Fig. 4c plots the detection of the axis of the Néel vector, the absolute direction remains unresolved. This information is revealed by combining the XMCD-PEEM and XMLD-PEEM in a four-color vector map shown in Fig. 4e, which plots the Boolean combination of linear and circular dichroism from Figs. 4c and d. The result reveals the

underlying altermagnetic Hall pseudovector in the real-space domain structure of the ultrathin BFO. As anticipated, the 4-fold symmetry of the altermagnetic domains in Fig. 4e is consistent with the d-wave altermagnetic symmetry from DFT (Figs. 4a and b).

Outlook

We present a design and synthesis pathway that preserves room-temperature multiferroic order down to ultrathin thicknesses. Atomic-resolution STEM and electron-ptychography polar-vector mapping reveal an enhanced out-of-plane to in-plane polarization ratio at the smallest scales. We observe a continuous, thickness-driven phase transition consistent with Kibble-Zurek-like behavior, during which multiferroic topological textures (vortices and vortex rings) emerge. At four unit cells, a collinear monoclinic *Cm* state is stabilized in which the long-wavelength cycloid is quenched and signatures of d-wave altermagnetism appear⁵². Taken together, these measurements provide a picture of real-space multiferroic topology at device-relevant thicknesses with d-wave altermagnetic time-reversal symmetry breaking signatures in the XMCD, DFT, and symmetry analysis. Beyond this specific material, the approach outlines a general blueprint for engineering ultrathin multiferroicity with multi-order-parameter topological textures, enabling voltage-based writing with symmetry-selective readout.

Methods

Molecular-Beam Epitaxy: All films (thicknesses 2-50 nm) were grown by reactive MBE in a Veeco GEN10 system using a mixture of 80% ozone (distilled) and 20% oxygen. SrRuO₃ bottom electrodes were grown using an elemental source of Sr and an e-beam Ru source at fluxes of 1×10^{13} atoms/cm²s and 3×10^{13} atoms/cm²s respectively. Elemental sources of Bi and Fe were used at fluxes of 1.5×10^{14} and 2×10^{13} atoms/cm²s, respectively, corresponding to a relative flux ratio of 8:1. To prevent Ru desorption from the surface, an initial Fe₂O₃ layer was deposited before co-deposition of both Bi and Fe. All films were grown at a substrate temperature of 675 °C as measured by an optical pyrometer operating at a wavelength of 980 nm and a chamber background pressure of 5×10^{-6} Torr.

Scanning Transmission electron microscopy: The cross-section samples were prepared using a FEI Helios 660 focused ion beam (FIB) with a gallium (Ga) ion beam source. After sample preparation, high-angle annular dark-field scanning transmission electron microscopy (HAADF-STEM) imaging were performed using an FEI Titan Themis G3 (scanning) transmission electron microscope equipped with double Cs-correctors operated at 300 kV. The convergence semi-angle is 25 mrad and the collection angle is 48-200 mrad.

Multislice Electron Ptychography: The four-dimensional STEM (4D-STEM) dataset was collected using a high dynamic-range electron microscope pixel array detector (EMPAD) with 128 x 128 pixel⁶¹. The scan step size is 0.349 Å and the acquisition time per diffraction pattern is 1 ms with an additional 0.86 ms readout time. A probe defocus of 10 nm was used to increase the real-space probe overlap area for data redundancy. The mixed-state, multislice electron ptychography method is based on a customized PtychoShelves package⁶², fold-slice⁶³⁻⁶⁶, to reconstruct phase information. Bayesian optimization⁶⁷ was first used to determine the defocus and sample thickness for generating the initial probe. Then the “Ptychographic Experiment and Analysis Robot” (PEAR)⁶⁸, a framework that leverages large language models (LLMs), was used to assist with the processing of the data.

Piezoresponse Force Microscopy: The ferroelectric domains in BFO were imaged by piezoresponse force microscopy (PFM) using Asylum Jupiter XR and MFP-3D Origin atomic force microscopes. Out-of-plane components of the polarization were imaged in DART mode and in-plane components were imaged in lateral mode.

Quadrature phase differential interferometer-based PFM: We used a commercially available Vero AFM system (from Asylum Research, an Oxford Instruments company) equipped with a quadrature phase differential interferometer (QPDI). We employed ADAMA commercially available single-crystal diamond probes (model AD-2.8-AS). The “null” spot of the cantilever, which mitigates electrostatic and cantilever dynamic artifacts, is found by moving the laser spot until the in-contact resonance frequency peak disappears, as explained in detail⁶⁹.

Scanning Nitrogen Vacancy Magnetometry: NV magnetometry measurements were performed using a Qnami Quantum Microscope–ProteusQTM. Parabolically tapered QuantileverTM MX+ diamond tips were employed for their high photon collection efficiency and superior signal-to-noise ratio, making them ideally suited for detecting the extremely weak stray magnetic fields characteristic of BFO. Each tip hosts a single negatively charged nitrogen–vacancy (NV[−]) center, consisting of a substitutional nitrogen atom adjacent to a carbon vacancy. The electronic ground state of the NV center is a spin triplet ($m_s = 0, \pm 1$), which forms the basis of the quantum sensor. In the experimental configuration, an external ring magnet is applied to lift the degeneracy of the $m_s = \pm 1$ sublevels. A microwave (MW) source is then swept in frequency to induce spin transitions ($m_s = 0 \leftrightarrow \pm 1$), which are detected optically via changes in the photoluminescence (PL) intensity, an effect known as optically detected magnetic resonance (ODMR). As the NV tip scans across the sample surface, local variations in the stray magnetic field (B) projected along the NV axis shift the ODMR resonance frequencies, thereby providing a spatial map of the magnetic field distribution. Two imaging modes were employed in this study: the dual iso-B mode and the full-B mode. In the dual

iso-B mode, the PL signal is recorded at two fixed MW frequencies chosen near the full width at half maximum (FWHM) of the ODMR line shape, and their difference [$PL(v_2) - PL(v_1)$] yields a high-contrast map of the local magnetic texture. In the full-B mode, the complete ODMR spectrum is acquired and fitted at each pixel, allowing a quantitative reconstruction of the local magnetic field magnitude with nanoscale spatial resolution.

The typical magnetic field sensitivity achievable under continuous-wave ODMR conditions with QuantileverTM MX+ diamond tips was on the order of $1.5\text{--}2.5 \mu\text{T Hz}^{-1/2}$. This limit arises from the interplay of shot-noise-limited photon detection, PL contrast, and laser- and microwave-induced broadening, and is consistent with the theoretical limit for this system⁷⁰. To overcome this limitation in the thinnest, 1.6 nm BFO sample, we also implemented pulsed ODMR measurements, wherein a π -pulse is used to drive the spin transition, while the MW field remains off during the spin readout window. This protocol eliminates laser-induced broadening and contrast degradation, allowing us to clearly resolve the hyperfine structure associated with the ¹⁴N nuclear spin. For quantitative imaging, we deliberately selected the central hyperfine resonance to ensure uniform signal response and optimal field sensitivity across the scan area.

Laboratory-based X-ray diffraction: To verify epitaxial growth, reciprocal space map (RSM) scans were performed on a Panalytical diffractometer with a Cu K-alpha source. RSMs were taken around the (332) DSO diffraction peak along the [001]₀ axis to access the (103)_{PC} BFO peaks.

Macroscopic XMLD Spectroscopy: Macroscopic X-ray Linear Dichroism (XLD) measurements were taken at the Advanced Light Source (ALS) at Lawrence Berkeley National Laboratory (LBNL) at beamline 4.0.2 at the Fe L₂-edge. Measurements were performed at both normal (90°) incidence and grazing (16°) incidence. We quantify the dichroic signal as XLD Intensity = $(I_p - I_s)/(I_p + I_s)$, where I_p and I_s are total electron yield (TEY) intensities for *p*- and *s*-polarized light.

Spatially resolved XMLD and XMCD PEEM Imaging: The X-ray PEEM measurements (and corresponding XMLD) were taken at the MAXPEEM end-station at the MAXIV synchrotron. The X-ray beam is incident normal to the sample surface, with the X-ray linear vector in the plane of the sample and the helicity vector out of plane. The X-Ray Magnetic Linear Dichroism is calculated using XLD Intensity = $(I(E_1) - I(E_2))/(I(E_1) + I(E_2))$, where I refers to the pixel intensity measured at the corresponding energies. For our case, E_1, E_2 corresponds to the two peaks of the L3 (or L2) absorption peak (see Extended Data Fig. 17). The XMCD, magnetic circular dichroism, was calculated via $XMCD = (I(\mu_+) - I(\mu_-))/(I(\mu_+) + I(\mu_-))$, where I refers to the pixel intensity measured at the corresponding helicities μ_{\pm} at a fixed energy. All measurements were taken at room temperature.

XMLD vector maps were created from a set of XMLD images ranging from $\theta = -90^\circ$ to $\theta = 90^\circ$ relative to the horizontal axis in steps of 10° . The angular dependance is fitted with $A \sin^2(\theta + \phi) + B$, where ϕ (the phase offset) describes the local Néel-vector axis (see Extended Data Fig 18). We further plot the histogram of the binned pixel values from the fit in a polar plot to illustrate the contributions to the XMLD signal (more information in Supplementary Discussion III) as in Figure 3. We note that we cannot resolve 180° reversal; i.e., the polar plot only contains information in 180° hemisphere. Finally, we binarize the XMLD (two states), then split each state by the sign of XMCD at that pixel, resulting in four unique states that represent four absolute orientations of the Néel vector (see Extended Data Fig. 19-20). Data analysis was done using the *athina* package⁷¹, as well as custom python functions. We note that crystal fields can also give rise to a XLD signal. This can be neglected here as the crystal structure is in approximation cubic, similar to previous studies on hematite, the parent compound of BFO^{49,50}.

First-Principles Calculations: Calculations were performed using DFT⁷² with the projector augmented wave (PAW) method⁷³ as implemented in the Vienna *ab initio* simulation package (VASP 5.4.4)⁷⁴. The structural relaxations are carried out using a Γ -centered k-point grid equivalent to an 8x8x8 sampling of

the five-atom unit cell Brillouin zone. The energy cutoff for the plane wave basis is set to 600 eV. The PAW potential corresponds to $5d^{10} 6s^2 6p^3$ valence electron configuration for Bi, $3p^6 3d^7 4s^1$ for Fe, $4p^6 4d^7 5s^1$ for Ru as well as $4s^2 4p^6 4d^{0.001} 5s^{1.999}$ and $2s^2 2p^4$ for Sr and oxygen, respectively. We employ the PBE + U and PBEsol + U functional form of the generalized gradient approximation⁷⁵, with a commonly used values of $U_{eff} = 4$ eV and 0.6 eV for the Fe and Ru 3d orbitals^{76,77} respectively, according to Dudarev's approach⁷⁸.

For structural relaxation in BFO/SRO bilayer setup, we also use Fermi smearing with smearing width $\sigma = 0.15$ eV and introduce electrostatic corrections to reduce the leading errors due to non-zero dipole moment under periodic boundary conditions^{79,80}. We do not impose any symmetry constraints during structural and electronic relaxations but fix the geometry of the three bottom-most SRO unit cell layers according to HAADF-STEM observations.

Acknowledgements:

Devices and films were processed using equipment in the Brown University Instrumentation for Molecular and Nanoscale Innovation facility. This research used resources of the Advanced Light Source, a U.S. DOE Office of Science User Facility under contract no. DE-AC02-05CH11231. **Funding:** Scanning nitrogen vacancy magnetometry measurements were supported by the Air Force Office of Scientific Research under FA9550-24-1-0169. BiFeO₃ synthesis and measurements were supported by NSF EPSCOR RII Track-4 Research Fellows Program under OIA-2327352 and under ETHOS MURI via cooperative agreement W911NF-21-2-0162. X.L. acknowledges support from the Rice Advanced Materials Institute (RAMI) at Rice University as a RAMI Postdoctoral Fellow. X.L. and Y.H. acknowledge support from NSF (FUSE-2329111 and CMMI-2239545) and Welch Foundation (C-2065). X.L. and Y.H. acknowledge the Electron Microscopy Center, Rice University. S. M. U. S., J. S., and A. W. acknowledge funding from the Deutsche Forschungsgemeinschaft (DFG, German Research Foundation) projects 268565370 (SFB TRR173 projects A09 and B14) and 465145163 (CRC 1552 project A02). LŠ acknowledges funding from the ERC Starting Grant No. 101165122 and Deutsche Forschungs- gemeinschaft (DFG) grant no. TRR 288 – 7422213477

(Projects A09 and B05). Quadrature phase differential interferometer-based PFM measurements were conducted as part of a user project at the Center for Nanophase Materials Sciences (CNMS), which is a US Department of Energy, Office of Science User Facility at Oak Ridge National Laboratory. L.B. also acknowledges the support of the Vannevar Bush Faculty Fellowship (VBFF) Grant No. N00014-20-1-2834 from the Department of Defense and ARA Impact Grant 3.0. We thank MAX IV Laboratory for time on beamline MaxPEEM under proposals 20230367, 20240599, 20241342, 20250678, 20250994 and 20251711. Research conducted at MAX IV, a Swedish national user facility, is supported by the Swedish Research Council under contract 2018-07152, the Swedish Governmental Agency for Innovation Systems under contract 2018-04969, and Formas under contract 2019-02496.

Author Contributions: L.C. led study and guided the team.; G.F., E.G., J.S., K.L, C.K., A.W, and L.C. performed all X-ray spectroscopy and imaging measurements.; X-ray spectroscopy was analyzed by G.F., E.G., S.M.U.S, A.W., under guidance from L.C. and A.W.; M.R. optimized the synthesis of BFO thin films and performed X-ray diffraction studies under guidance from D.G.S. and L.C.; X.L. performed all STEM measurements and analysis under the supervision of Y.H.; A.G. and M.R. performed NV magnetometry and PFM with the help of S.O., S.Z., and A.Q., under the supervision of R.R., P.S., and L.C. Quadrature phase differential interferometer -based PFM was performed by M.C.; First principles calculations were performed by S.P. and Y.N., as well as J.P. and F.C.F.M. under supervision of L.S.; The manuscript was prepared by L.C., A.W., G.F., P.M., P.S., M.R., X.L., L.S., S.P., L.B., and R.R.; All authors contributed to the discussion of the data in the manuscript and the supplementary materials.

Competing interests: The authors declare no competing interests.

References

1. Park, J. H. *et al.* Magnetic Properties at Surface Boundary of a Half-Metallic Ferromagnet La_{0.7}Sr_{0.3}MnO₃. *Phys. Rev. Lett.* **81**, 1953 (1998).
2. Sun, J. Z., Abraham, D. W., Rao, R. A. & Eom, C. B. Thickness-dependent magnetotransport in ultrathin manganite films. *Appl. Phys. Lett.* **74**, 3017–3019 (1999).
3. Borges, R. P., Guichard, W., Lunney, J. G., Coey, J. M. D. & Ott, F. Magnetic and electric “dead” layers in (La_{0.7}Sr_{0.3})MnO₃ thin films. *J. Appl. Phys.* **89**, 3868–3873 (2001).
4. Mehta, R. R., Silverman, B. D. & Jacobs, J. T. Depolarization fields in thin ferroelectric films. *J. Appl. Phys.* **44**, 3379–3385 (1973).
5. Fong, D. D. *et al.* Ferroelectricity in ultrathin perovskite films. *Science* **304**, 1650–1653 (2004).
6. De Luca, G. *et al.* Nanoscale design of polarization in ultrathin ferroelectric heterostructures. *Nat. Commun.* **2017** *81* **8**, 1–7 (2017).
7. Junquera, J. & Ghosez, P. Critical thickness for ferroelectricity in perovskite ultrathin films. *Nat. 2003* **4226931** **422**, 506–509 (2003).
8. Tybella, T., Ahn, C. H. & Triscone, J. M. Ferroelectricity in thin perovskite films. *Appl. Phys. Lett.* **75**, 856–858 (1999).
9. Gao, P. *et al.* Possible absence of critical thickness and size effect in ultrathin perovskite ferroelectric films. *Nat. Commun.* **8**, 1–8 (2017).
10. Maksymovych, P. *et al.* Ultrathin limit and dead-layer effects in local polarization switching of BiFeO₃. *Phys. Rev. B* **85**, 014119 (2012).
11. Huijben, M. *et al.* Ultrathin Limit of Exchange Bias Coupling at Oxide Multiferroic/Ferromagnetic Interfaces. *Adv. Mater.* **25**, 4739–4745 (2013).
12. Gradauskaitė, E. *et al.* Defeating depolarizing fields with artificial flux closure in ultrathin ferroelectrics. *Nat. Mater.* **2023** 1–7 (2023) doi:10.1038/s41563-023-01674-2.
13. Stengel, M., Vanderbilt, D. & Spaldin, N. A. Enhancement of ferroelectricity at metal-oxide interfaces. *Nat. Mater.* **8**, 392–397 (2009).

14. Béa, H. *et al.* Ferroelectricity Down to at Least 2 nm in Multiferroic BiFeO₃ Epitaxial Thin Films. *Jpn. J. Appl. Phys.* **45**, L187 (2006).
15. Kuo, C. Y. *et al.* Single-domain multiferroic BiFeO₃ films. *Nat. Commun.* **7**, 1–7 (2016).
16. Ji, D. *et al.* Freestanding crystalline oxide perovskites down to the monolayer limit. *Nature* **570**, 87–90 (2019).
17. Strkalj, N. *et al.* In-situ monitoring of interface proximity effects in ultrathin ferroelectrics. *Nat. Commun. 2020* **11** 1–6 (2020).
18. Wang, H. *et al.* Direct observation of room-temperature out-of-plane ferroelectricity and tunneling electroresistance at the two-dimensional limit. *Nat. Commun. 2018* **9** 3319- (2018).
19. Mundy, J. A. *et al.* Atomically engineered ferroic layers yield a room-temperature magnetoelectric multiferroic. *Nature* **537**, 523–527 (2016).
20. Ye, B. *et al.* Reducing the magnetic dead layer to one unit cell in ultrathin films of manganites using spin-orbit coupling. *Phys. Rev. B* **108**, 094406 (2023).
21. Guo, E. J. *et al.* Removal of the Magnetic Dead Layer by Geometric Design. *Adv. Funct. Mater.* **28**, 1800922 (2018).
22. Chen, Y. *et al.* Significant Reduction of the Dead Layers by the Strain Release in La_{0.7}Sr_{0.3}MnO₃ Heterostructures. *ACS Appl. Mater. Interfaces* **14**, 39673–39678 (2022).
23. Ying-Hao Chu, B. *et al.* Nanoscale Domain Control in Multiferroic BiFeO₃ Thin Films. *Adv. Mater.* **18**, 2307–2311 (2006).
24. Heron, J. T. *et al.* Deterministic switching of ferromagnetism at room temperature using an electric field. *Nature* **516**, 370–373 (2014).
25. Wang, H. *et al.* Overcoming the Limits of the Interfacial Dzyaloshinskii–Moriya Interaction by Antiferromagnetic Order in Multiferroic Heterostructures. *Adv. Mater.* 1904415 (2020) doi:10.1002/adma.201904415.
26. Aso, R., Kan, D., Shimakawa, Y. & Kurata, H. Atomic level observation of octahedral distortions at the perovskite oxide heterointerface. *Sci. Reports* **2013** **3**, 2214- (2013).

27. Rondinelli, J. M., May, S. J. & Freeland, J. W. Control of octahedral connectivity in perovskite oxide heterostructures: An emerging route to multifunctional materials discovery. *MRS Bull.* **37**, 261–270 (2012).
28. Yao, X. *et al.* Control of ferroelectric polarization in BiFeO₃ bilayer films through interface engineering. *npj Quantum Mater.* **2025 101** **10**, 40- (2025).
29. Lee, S. S. *et al.* Correlation between Geometrically Induced Oxygen Octahedral Tilts and Multiferroic Behaviors in BiFeO₃ Films. *Adv. Funct. Mater.* **28**, 1800839 (2018).
30. Puggioni, D., Giovannetti, G. & Rondinelli, J. M. Polar metals as electrodes to suppress the critical-thickness limit in ferroelectric nanocapacitors. *J. Appl. Phys.* **124**, 55 (2018).
31. Diéguez, O., González-Vázquez, O. E., Wojdeł, J. C. & Íñiguez, J. First-principles predictions of low-energy phases of multiferroic BiFeO₃. *Phys. Rev. B - Condens. Matter Mater. Phys.* **83**, 094105 (2011).
32. Christen, H. M., Nam, J. H., Kim, H. S., Hatt, A. J. & Spaldin, N. A. Stress-induced R-MA-MC-T symmetry changes in BiFeO₃ films. *Phys. Rev. B* **83**, 144107 (2011).
33. Rahmedov, D., Wang, D., Añiguez, J. & Bellaiche, L. Magnetic cycloid of BiFeO₃ from atomistic simulations. *Phys. Rev. Lett.* **109**, 037207 (2012).
34. Ramazanoglu, M. *et al.* Local weak ferromagnetism in single-crystalline ferroelectric BiFeO₃. *Phys. Rev. Lett.* **107**, 207206 (2011).
35. Kadomtseva, A. M., Zvezdin, A. K., Popov, Y. F., Pyatakov, A. P. & Vorob'Ev, G. P. Space-time parity violation and magnetoelectric interactions in antiferromagnets. *JETP Lett.* **79**, 571–581 (2004).
36. Haykal, A. *et al.* Antiferromagnetic textures in BiFeO₃ controlled by strain and electric field. *Nat. Commun.* **11**, 1704 (2020).
37. Meisenheimer, P. *et al.* Switching the spin cycloid in BiFeO₃ with an electric field. *Nat. Commun.* **2024 151** **15**, 1–8 (2024).
38. Zhao, T. *et al.* Electrical control of antiferromagnetic domains in multiferroic BiFeO₃ films at

room temperature. *Nat. Mater.* **5**, 823–829 (2006).

39. Moubah, R. *et al.* Direct imaging of both ferroelectric and antiferromagnetic domains in multiferroic BiFeO₃ single crystal using x-ray photoemission electron microscopy. *Appl. Phys. Lett.* **100**, 15 (2012).

40. Butcher, T. A. *et al.* Ptychographic nanoscale imaging of the magnetoelectric coupling in freestanding BiFeO₃. (2023).

41. Gross, I. *et al.* Real-space imaging of non-collinear antiferromagnetic order with a single-spin magnetometer. *Nat. 2017 5497671* **549**, 252–256 (2017).

42. Meisenheimer, P. *et al.* Switching the spin cycloid in BiFeO₃ with an electric field. *Nat. Commun.* **15**, 1–8 (2024).

43. He, Q. *et al.* Magnetotransport at Domain Walls in BiFeO₃. *Phys. Rev. Lett.* **108**, 067203 (2012).

44. Gareeva, Z., Diéguez, O., Íñiguez, J. & Zvezdin, A. K. Complex domain walls in BiFeO₃. *Phys. Rev. B* **91**, 060404 (2015).

45. Ghosal, A. *et al.* Low-energy domain wall racetracks with multiferroic topologies. *ArXiv* (2025) doi:arXiv:2507.12633.

46. Lebeugle, D. *et al.* Electric-field-induced spin flop in BiFeO₃ single crystals at room temperature. *Phys. Rev. Lett.* **100**, 1–4 (2008).

47. Kibble, T. W. B. Topology of cosmic domains and strings. *J. Phys. A. Math. Gen.* **9**, 1387 (1976).

48. Zurek, W. H. Cosmological experiments in superfluid helium? *Nature* **317**, 505–508 (1985).

49. Jani, H. *et al.* Antiferromagnetic half-skyrmions and bimerons at room temperature. *Nature* **590**, 74–79 (2021).

50. Chmiel, F. P. *et al.* Observation of magnetic vortex pairs at room temperature in a planar α -Fe₂O₃/Co heterostructure. *Nat. Mater.* **17**, 581–585 (2018).

51. Urru, A. *et al.* G-type antiferromagnetic BiFeO₃ is a multiferroic g-wave altermagnet. *Phys. Rev. B* **112**, 104411 (2025).

52. Šmejkal, L. Altermagnetic multiferroics and altermagnetoelectric effect. *ArXiv* 1–6 (2024).

53. Duan, X. *et al.* Antiferroelectric Altermagnets: Antiferroelectricity Alters Magnets. *Phys. Rev. Lett.* **134**, 106801 (2025).

54. Husain, S. *et al.* Anisotropic magnon transport in an antiferromagnetic trilayer heterostructure: is BiFeO₃ an altermagnet? (2026).

55. Šmejkal, L., Sinova, J. & Jungwirth, T. Beyond Conventional Ferromagnetism and Antiferromagnetism: A Phase with Nonrelativistic Spin and Crystal Rotation Symmetry. *Phys. Rev. X* **12**, 031042 (2022).

56. Gu, M. *et al.* Ferroelectric Switchable Altermagnetism. *Phys. Rev. Lett.* **134**, 106802 (2025).

57. Hariki, A. *et al.* X-Ray Magnetic Circular Dichroism in Altermagnetic α -MnTe. *Phys. Rev. Lett.* **132**, 176701 (2024).

58. Amin, O. J. *et al.* Nanoscale imaging and control of altermagnetism in MnTe. *Nature* **636**, 348–353 (2024).

59. Galindez-Ruales, E. *et al.* Revealing the Altermagnetism in Hematite via XMCD Imaging and Anomalous Hall Electrical Transport. *Adv. Mater.* **37**, e05019 (2025).

60. Šmejkal, L. *et al.* Crystal time-reversal symmetry breaking and spontaneous Hall effect in collinear antiferromagnets. *Sci. Adv.* **6**, eaaz8809 (2020).

61. Tate, M. W. *et al.* High Dynamic Range Pixel Array Detector for Scanning Transmission Electron Microscopy. *Microsc. Microanal.* **22**, 237–249 (2016).

62. Wakonig, K. *et al.* PtychoShelves, a versatile high-level framework for high-performance analysis of ptychographic data. *J. Appl. Crystallogr.* **53**, 574–586 (2020).

63. Thibault, P. *et al.* High-Resolution Scanning X-ray Diffraction Microscopy. *Science (80-.)* **321**, 379–382 (2008).

64. Suzuki, A., Niida, Y., Joti, Y., Thibault, P. & Guizar-Sicairos, M. Maximum-likelihood refinement for coherent diffractive imaging. *New J. Phys.* **14**, 063004 (2012).

65. Thibault, P. & Menzel, A. Reconstructing state mixtures from diffraction measurements. *Nature* **494**, 68–71 (2013).

66. Usov, I., Tsai, E. H. R., Guizar-Sicairos, M., Menzel, A. & Diaz, A. X-ray ptychography with extended depth of field. *Opt. Express*, Vol. 24, Issue 25, pp. 29089-29108 **24**, 29089–29108 (2016).

67. Cao, M. C., Chen, Z., Jiang, Y. & Han, Y. Automatic parameter selection for electron ptychography via Bayesian optimization. *Sci. Rep.* **12**, 1–10 (2022).

68. Yin, X., Shi, C., Deng, J., Han, Y. & Jiang, Y. PEAR: A Knowledge-guided Autonomous Pipeline for Ptychography Enabled by Large Language Models. *Microsc. Microanal.* **30**, 402–403 (2024).

69. Collins, L., Liu, Y., Ovchinnikova, O. S. & Proksch, R. Quantitative Electromechanical Atomic Force Microscopy. *ACS Nano* **13**, 8055–8066 (2019).

70. Dréau, A. *et al.* Avoiding power broadening in optically detected magnetic resonance of single NV defects for enhanced dc magnetic field sensitivity. *Phys. Rev. B* **84**, 195204 (2011).

71. Golias, E. *athina*. (2024).

72. Kohn, W. & Sham, L. J. Self-Consistent Equations Including Exchange and Correlation Effects. *Phys. Rev.* **140**, A1133 (1965).

73. Blöchl, P. E. Projector augmented-wave method. *Phys. Rev. B* **50**, 17953 (1994).

74. Kresse, G. & Furthmüller, J. Efficient iterative schemes for ab initio total-energy calculations using a plane-wave basis set. *Phys. Rev. B* **54**, 11169 (1996).

75. Perdew, J. P., Burke, K. & Ernzerhof, M. Generalized Gradient Approximation Made Simple. *Phys. Rev. Lett.* **77**, 3865 (1996).

76. Neaton, J. B., Ederer, C., Waghmare, U. V., Spaldin, N. A. & Rabe, K. M. First-principles study of spontaneous polarization in multiferroic BiFeO₃. *Phys. Rev. B - Condens. Matter Mater. Phys.* **71**, 014113 (2005).

77. Shenton, J. K., Bowler, D. R. & Cheah, W. L. Effects of the Hubbard U on density functional-based predictions of BiFeO₃ properties. *J. Phys. Condens. Matter* **29**, 445501 (2017).

78. Dudarev, S. L., Botton, G. A., Savrasov, S. Y., Humphreys, C. J. & Sutton, A. P. Electron-energy-loss spectra and the structural stability of nickel oxide: An LSDA+U study. *Phys. Rev. B* **57**,

1505–1509 (1998).

79. Neugebauer, J. & Scheffler, M. Adsorbate-substrate and adsorbate-adsorbate interactions of Na and K adlayers on Al(111). *Phys. Rev. B* **46**, 16067 (1992).
80. Makov, G. & Payne, M. C. Periodic boundary conditions in ab initio calculations. *Phys. Rev. B* **51**, 4014 (1995).

Figures

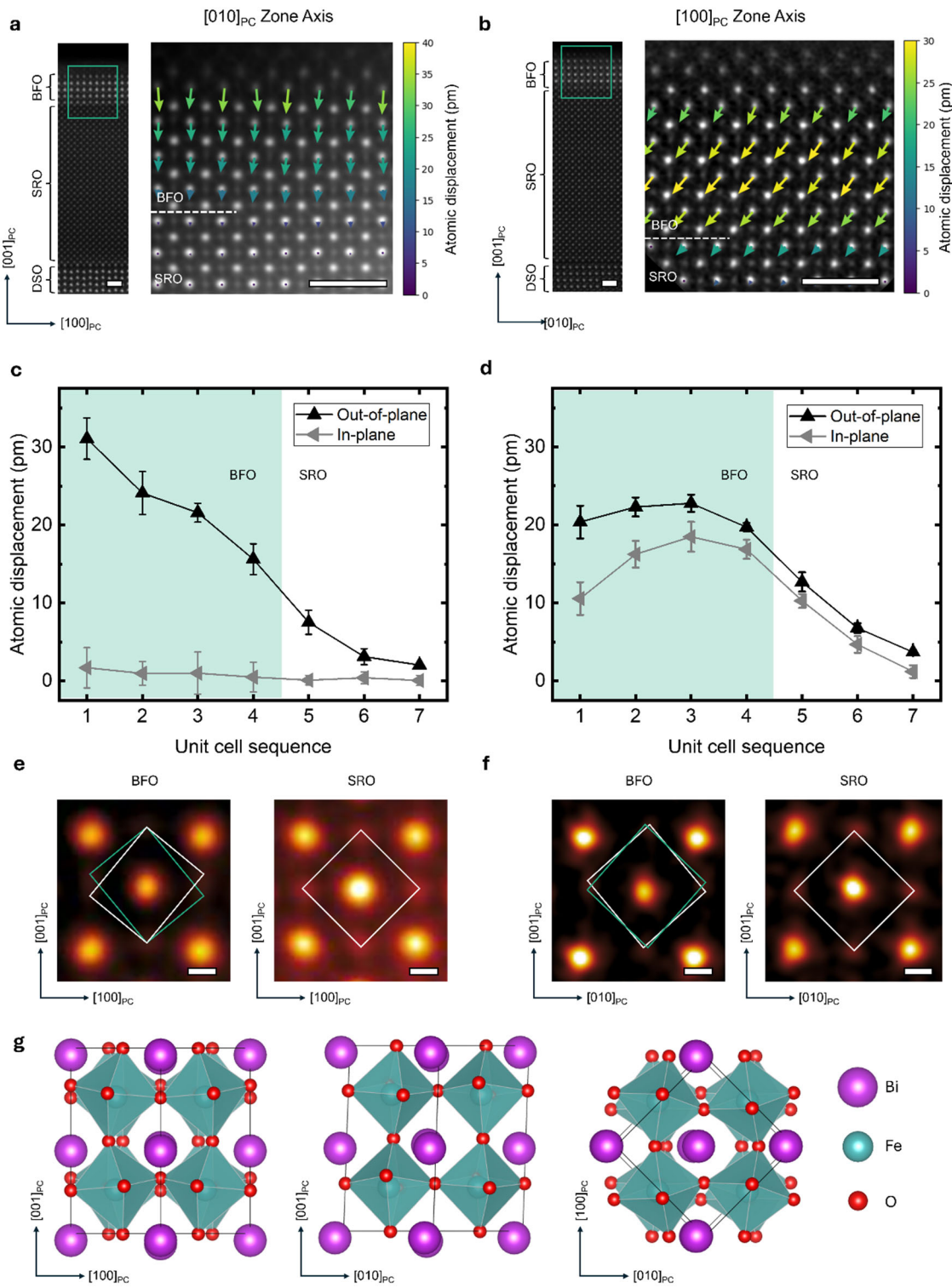


Figure 1 | Monoclinic structure and retained polar order in ultrathin BiFeO₃ (BFO). Atomically resolved high-angle annular dark-field scanning transmission electron microscopy (HAADF-STEM) and

multislice electron ptychography-based polar vector mapping in 4 unit cell BFO grown on DyScO₃ with SrRuO₃ (SRO) bottom electrodes along the **a**) [010]_{PC} and **b**) [100]_{PC} zone axes. Scale bars in (a) and (b) are 1 nm. **c,d**) Out-of-plane and in-plane atomic displacement mapping of the ptychographic phase images shown in (a) and (b), respectively, across the BFO/SRO interface. No ferroelectric dead layer and induced polarization in the SRO is observed. **e,f**) Expanded view of the unit cell of BFO (SRO), illustrating the octahedral tilt pattern present (absent) along each in plane zone axis. Scale bars in (e) and (f) are 1 Å. **g**) Unit cell of the relaxed *Cm* phase obtained from DFT simulations with bulk BFO setting.

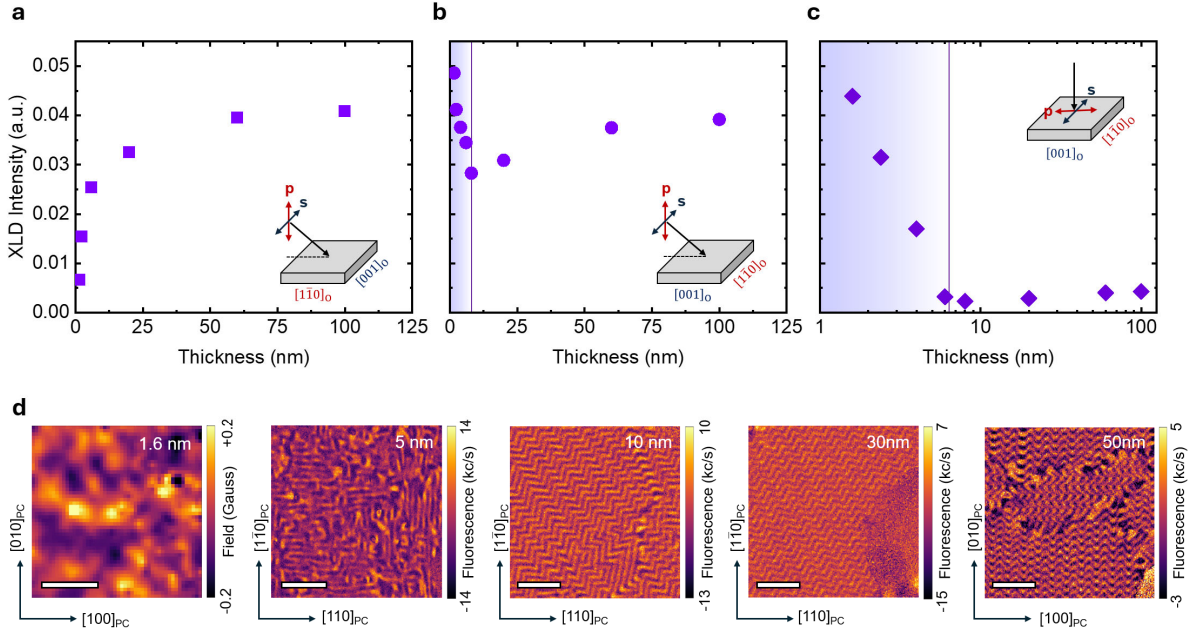


Figure 2 | Retained collinear magnetic order in ultrathin BiFeO₃ (BFO). Fe L₂ X-ray linear dichroism (XLD) at grazing incidence (16°) along the **a**) [001]_o and **b**) [1-10]_o substrate directions as a function of thickness in BFO/SrRuO₃(20 nm)/DSO heterostructures. Fe L₂ XLD in BFO is predominately sensitive to magnetic order. **c**) Fe L₂ XLD thickness scaling at normal incidence in the same heterostructure as (a) and (b). Insets show the orientation of X-ray light polarization relative to the sample. **d**) High resolution scanning nitrogen vacancy magnetometry as a function of BFO thickness. The 1.6 nm sample was probed using pulsed optically detected magnetic resonance, whereas the rest correspond to iso-magnetic field imaging (Methods). The scale bars in (d) are 500 nm, except the 1.6 nm sample, where it is 250 nm. a.u., arbitrary units.

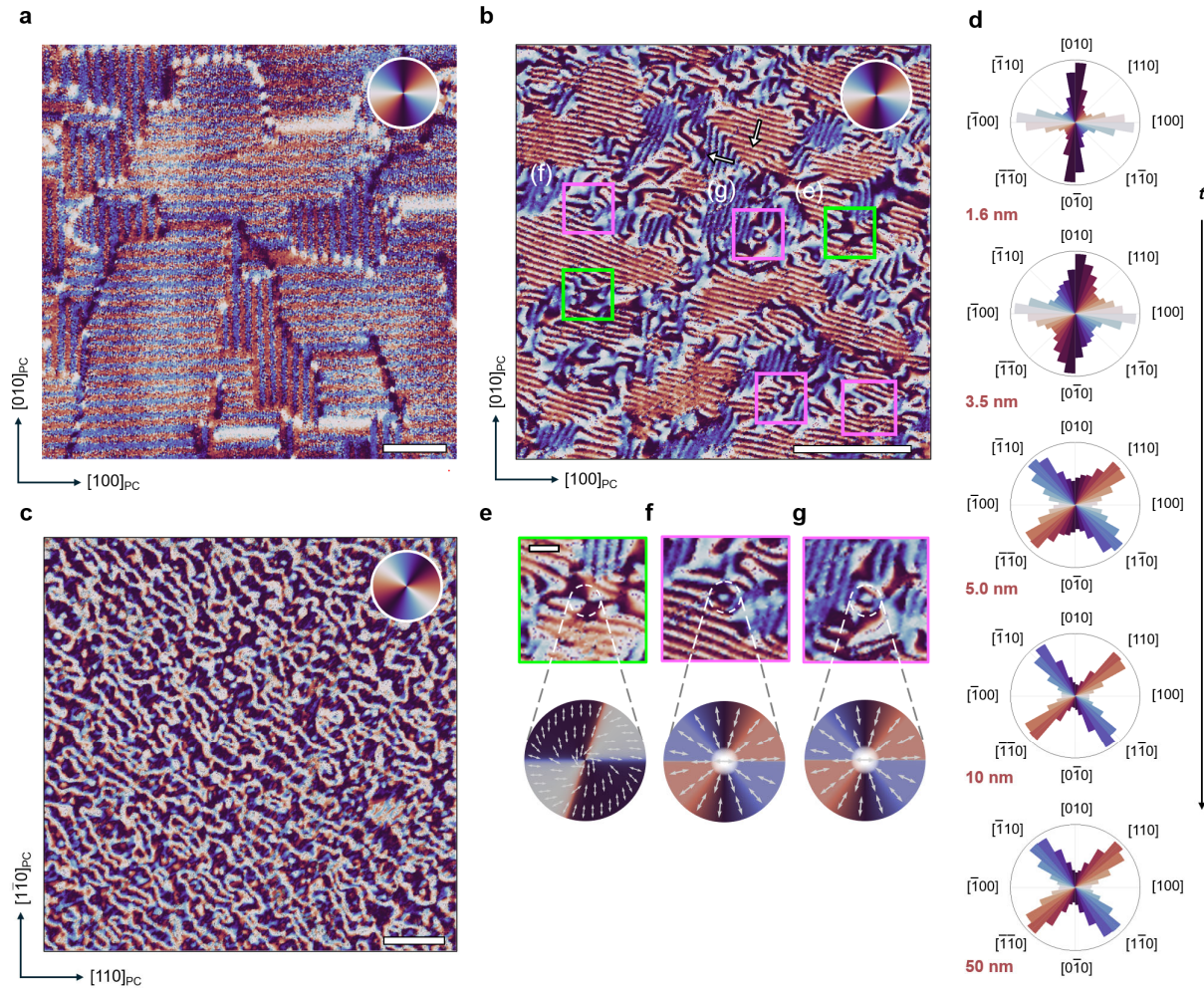


Figure 3 | Emergent multiferroic topology in thin BiFeO_3 (BFO). **a)** Fe L_3 edge normal incidence X-ray linear dichroism – photo emission electron microscopy (XLD-PEEM) in-plane vector map of **a)** 50 nm, **b)** 3.5 nm, and **c)** 1.6 nm of BiFeO_3 grown on DyScO_3 with SrRuO_3 bottom electrodes. Fe L_3 edge XLD in BFO is sensitive to both polar and antiferromagnetic (AFM) order. Inset color wheels show the orientation of each order parameter with red/blue contrast corresponding to polar order and purple/white contrast corresponding to AFM order. Scale bars in (a)-(c) are 1 μm . **d)** Order parameter radial histograms extracted from the fit of the vector maps for various thicknesses (t) of BFO (Methods). Exemplary topological defects from colored boxes in (b) are highlighted in **e)-g)** showing vertex and vertex rings forming during the continuous phase transition. The scale bar in (e)-(g) is 200 nm.

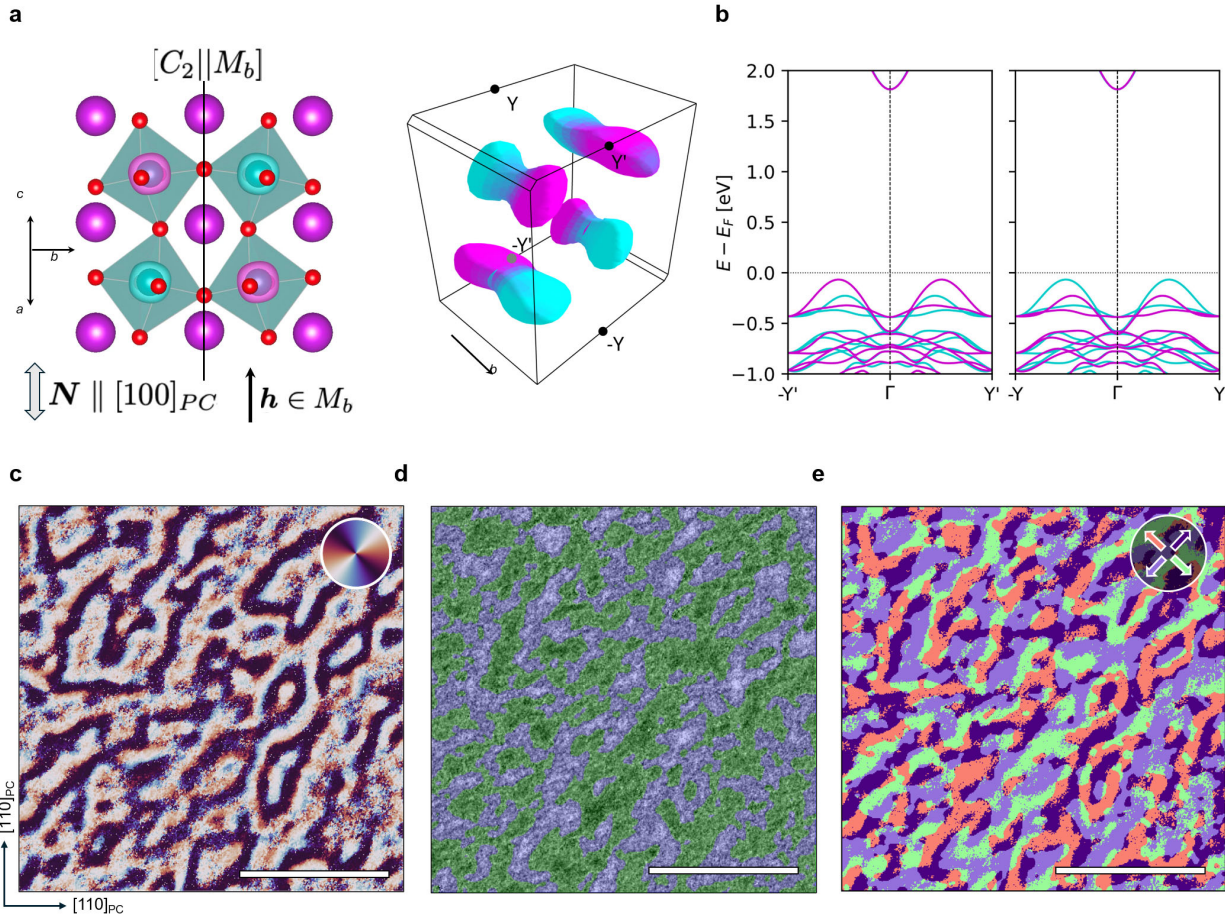


Figure 4 | Altermagnetic signatures in ultrathin BiFeO_3 (BFO). **a)** Crystallographic structure and DFT calculated altermagnetic spin density of the thin film Cm BFO with a G-type antiferromagnetic dipolar order. The opposite spin channels (marked by magenta and cyan color) are related by altermagnetic spin group symmetry $[C_2||M_b]$, combining two-fold spin rotation C_2 with a black mirror plane M_b along the crystallographic b -direction. **b)** Momentum space altermagnetism of Cm BFO. Left: DFT calculated constant energy isosurfaces in Brillouin zone at -0.08 eV from the top of the valence band. The spin polarization calculated on top of the constant energy isosurface shows altermagnetic d-wave symmetry. Right: Nonrelativistic altermagnetic spin-splitting in the bandstructure calculated from DFT. The spin splitting confirms the altermagnetic (i) d-wave symmetry as it alternates in sign along the $-Y'Y$ and $-YY'$ directions (notation marked in the Brillouin zone shown in the left panel), and (b) time-reversal symmetry breaking as the spin is the same for opposite wavevectors. The altermagnetic T breaking allows for XMCD and Hall vector \mathbf{h} in the mirror plane when the Néel vector \mathbf{N} is oriented along \mathbf{b} direction as marked in panel a) **c)** XLD-PEEM vector map and **d)** XMCD PEEM imaging of the 1.6 nm BFO sample taken at normal incidence at the Fe L_3 edge (Methods, see Supplemental Discussion III-IV). **e)** XMCD binary mask of the XLD vector map with each color corresponding to four absolute orientations of the Néel vector. All scale bars are 0.5 μm .